Exploratory Description of Low Frequency Ocean Temperature Variability and Its Global Structure

Carl Wunsch*

Department of Earth and Planetary Sciences

Harvard University

Cambridge MA 02138

*Also Department of Earth, Atmospheric and Planetary Sciences, MIT

ABSTRACT

An exploratory description is made of nearly global potential temperature variability from to months to 20 years using the field derived from the ECCOv4 state estimate. Relative to higher frequencies, longer periods do not exhibit simplification in the space-time structures. Frequency spectra at individual points are usefully described by a reduced form of a previously proposed analytic model. In contrast, the vertical structure of the variability at low frequencies–periods beyond 1 year—has a very complex form, with only a few global generalizations apparent. Meridional wavenumber spectra, reflecting the dominant zonality of oceanic low frequencies, are spatially comparatively simple, while the zonal wavenumber spectra are spatially complex and not very meaningful. The emergence of strong spatial structures at longer periods is consistent with the presence of complex time-mean (0 frequency) structures in bottom topography, sidewalls, and meteorological forcing.

1. Introduction

This paper began as an attempt to realistically calculate the accuracies and precisions of published estimates of global mean oceanic temperature (heat content) change through time. As quickly became clear, the uncertainties of those calculations are dominated by the under-sampling of space-time structures of low-frequency oceanic thermal variability. That in turn led to the need to describe quantitatively the variability on a global scale at periods extending out to decades. No such previously published description appears to exist. Thus what follows is a draft description of low frequency oceanic thermal variability extending to 20-years duration. This effort raises fundamental questions about how to describe (and then to understand and use) in a basic form, the complex structure of a globally time and space varying fluid—if it is possible.

As will be seen, a large number of assumptions are necessary to proceed, and as a strawman, it would be no surprise to find major future changes being made in the results. In the meantime, the description does have exemplary uses both for the heat content problem and as tests of numerical models directed at the ocean in climate. Application of the results to the estimates of heat content change will be described elsewhere (Wunsch 2019).

As global data sets and global general circulation models with quantifiable skill have emerged over the past few decades, the conclusion that the ocean has a very strong regional and temporal complexity has become inescapable. Such technically beautiful ideas such as Sverdrup balance, abyssal recipes, Stommel-Arons flows, et al., are increasingly perceived to have at best regional applicability. Nonetheless a search for widely applicable principles describing oceanic physics is worthwhile. So for example, Sonnewald et al. (2019), using a vertically integrated vorticity balance, divided the ocean laterally into 6+ distinct dynamical regions, of greatly varying area.

Similarly, the altimetric wave number power law results of Xu and Fu (2012) seem to imply a minimum of about 14 dynamical regimes.

Representations via spectral methods are both a useful summary description and have many potential applications, depending upon the particular physical variable. The most familiar of such spectra, in frequency, wavenumber, or both, are those describing surface gravity waves (e.g., Komen et al. 1994) and the internal wave spectrum in the various Garrett and Munk (GM) estimates (Munk 1981 and many subsequent papers, e.g., Polzin and Lvov (2011).

For the mesoscale, as documented in numerous publications, no universality comparable to that seen for internal waves is found. In particular, the energy levels, as determined primarily from altimetric data, vary by more than two orders of magnitude (e.g., Hughes et al. 2018; their Fig. 1). A spectral representation has many useful applications, at least in a local sense. For Gaussian processes stationary in both space and time, the spectral representation along with the various mean values, is a complete description of the stochastic field. Here, the spatial inhomogeneity means that the frequency-wavenumber spectrum is not, even for purely Gaussian data, a complete stochastic representation—it is the first term in a higher order series. Nonetheless, its descriptive power, at least locally, remains useful. As one example, Fig. 1 shows the histogram of monthly potential temperature anomalies (relative to the 20-year mean) at one depth (477m) from an oceanic state estimate (e.g., Fukumori et al. 2018) described below. Although no formal test of normality has been made, the near- symmetric, unimodal distribution permits a ready interpretation of standard deviations and variances.

The focus here is on the temperature spectrum, because it is a scalar, has a very long history of in situ measurements, is important climatologically and is, in recent times in the upper ocean, widely sampled by the Argo array. But direct observations of deep (below about 2000m) interannual variability are very few —in a volume of roughly half the ocean. What follows relies on those data that do exist, and on the physics connecting the upper and abyssal oceans. Results are considered "exploratory" both because the full skill of the estimates at the longest periods is not known, and the best way to describe and use the resulting complicated behavior of a time-varying three-space-dimensional global field is also unclear.

2. The State Values and Their Frequency Spectra

Wortham and Wunsch (2014; hereafter WW14) proposed a general form of a three-space-dimension and time-spectrum for low frequency (below the Coriolis frequency, f) oceanic variability and compared it to a variety of data, both altimetric and from in situ measurements.

Their form followed on earlier discussions of Zang and Wunsch (2001; hereafter ZW01). WW14 showed a quantitatively useful fit to a wide variety of data, including altimetry, and from moored measurements of temperature and velocity. Subsequent developments for analogous statistical descriptions include Wortham et al. (2014); Abernathey and Wortham (2015); Samelson et al. (2016). Altimetry data have dominated the discussion of the wavenumber components of the spectrum, although for high wavenumbers (wavelengths shorter than about 100-200km), considerable deviation from a universal form is known (e.g., Xu and Fu 2012, but see Callies and Wu 2019, for discussion of their interpretation). Here the WW14 form is used to describe the temperature temporal-frequency spectrum so as to draw some near-global conclusions.

The values used here are from the twenty-year time-varying subset climatology of the Estimating the Circulation and Climate of the Ocean version 4 (ECCOv4) state estimate (see e.g., Fukumori et al. 2018 and references there). This climatology represents a weighted least-squares fit of the MITgcm (Marshall et al. 1997) and its evolutionary ECCO successors, to the diverse near-global data sets and meteorological forcing estimates that became available during and after the World Ocean Circulation Experiment. The single most important feature of this model representation is that the model is *free* running but with its numerous control parameters having been previously adjusted so that the model trajectory takes it through all of the data points within (mostly) estimates of their uncertainties.

As with many global analyses, the chief obstacle here is that the model is non-eddy-resolving (with a 1 degree of longitude and a variable latitude grid). Thus the strong assumption is, nonetheless, made here that the solution fit on periods exceeding several months and wavelengths exceeding ≈ 200km provides a quantitative estimate of the variability, its nature and structure. That assumption in turn rests upon the supposition that the dominant quasi-geostrophic nature of the ocean circulation is well-captured by the data—and hence the adjusted model—at long periods—an inference consistent with the comparisons to moored data in WW14. In particular, those authors showed that frequency spectra within the eddy band appeared to be smooth extensions of the spectra at lower frequencies. Hence one of the assumptions made here is that the low frequency results can be extrapolated into the eddy band.

To the extent that low frequency features produced e.g., by eddy-eddy or eddy-mean flow interactions, remain in thermal wind balance, the state estimate will properly represent them. The assumption is equivalent to the assertion that away from boundaries,

$$\frac{\partial}{\partial t}\left(f\frac{\partial v}{\partial z}-g\frac{\partial \rho}{\partial x}\right)=O(\varepsilon) \tag{1}$$

where ε is a small number relative to the left-hand-side terms and the fields are varying over years and longer. Boundary layers are not properly resolved with the existing resolution and a further assumption is that the unresolved regions are passively consistent with the strongly constrained, quasi-geostrophic, interior circulation and structure (an assumption underlying the Stommel-Arons picture). Penduff et al. (2010) and others show the integrated effects of eddies on the large-scale circulation; the extent to which a geostrophic pressure field is induced to balance that circulation is not clear. Balanced eddy structures, particularly those associated with topographic features, can persist for periods much exceeding a year (no low-frequency cut-off is known), and should future studies show major ageostrophic physics in eddy-resolving runs at low frequencies, what follows would have to be re-evaluated.

Frequency Spectra of the State Estimate

From the monthly average values of ECCOv4 at 477m the spectral density ranging from 20 years to 2 months (the Nyquist period) is readily computed as a function of frequency ω'. A depth of 477m was chosen as a reasonable global compromise value lying primarily below the mixed layer and above the main thermocline. The standard deviation of monthly anomalies averaged over 20 years at that depth is shown in Fig. 1. Converted to power, spectra sum to the squares of these values.

The discussion that follows is restricted to the region northward of 40°S, as the Southern Ocean with its strong mean advecting eastward flow is spectrally distinct from the remaining oceans (WW14). To the north, the sea ice region poleward of about 55°N is also omitted. This restriction still leaves many special dynamical regions in the domain, including the tropics. Conventional spectral estimates using a Daniell (rectangular frequency or wavenumber) window were computed for 27,634 distinct locations where the depth was at least 500m. An estimated $\nu = 6$ degrees of freedom was used at each spectral estimate frequency. The median (not area weighted) of all of these spectra can be seen in Fig. 2. In many locations, and as appears in the median result, the annual cycle and sometimes its harmonics, is conspicuous. In the net power and fitting results, these peaks are ignored because fitting without them changed the results only slightly. Its presence may be compensatory for a possible underestimate of power between two months and a year. The median power at 477m is $0.10(°\mathrm{C})^2 = (0.31\ ^o\mathrm{C})^2$ from 20 years to two months. A rough description would be that it has a ω'^{-2} behavior at frequencies above the annual cycle, and is flattened, tending toward white noise, at lower frequencies. The whitish character is consistent with the absence of strong (relative to the variability) data trends. A separate study of the temperature annual cycle and its overtones would be worthwhile.

The Analytic Spectrum

The WW14 spectrum is an empirical one for the interior ocean only, whose construction was guided only by general discussions both in theory and observation of wavenumber and frequency behavior (e.g., Vallis 2017; Arbic et al. 2012; Scott et al. 2017). In local Cartesian horizontal coordinates and time, it is of the form,

$$\Phi_\psi\left(k', l', \omega', x, y\right) = \tag{2}$$
$$A\left\{\frac{1}{\left(k'^2L_x^2 + l'^2L_y^2 + 1\right)^\alpha\left(\omega'^2T^2 + 1\right)} + \exp\left(-\left[k'^2L_x^2 + l'^2L_y^2 + T^2(k'c_x + l'c_y - \omega')^2\right]\right)\right\}.$$

Here, k', l', ω' are *non-radian* wavenumbers and frequencies, L_x, L_y, T are the zonal and meridional spatial scales and a temporal scale. c_x, c_y are empirical phase speeds, $\alpha \approx 5/2$. A is an adjustable overall magnitude. As discussed by WW14, all these parameters are functions of position—so that using local Cartesian coordinates makes some sense. Dependence upon x, y is slowly varying by assumption and the coordinates are usually suppressed below, but are implicit. The subscript ψ denotes the stream function as defined by ZW01. Each physical variable, be it temperature, salinity, surface elevation, velocity has a differing power density spectrum where a multiplying factor converts Φ_ψ into the applicable form. Thus the temperature spectrum would be,

$$\Phi_\theta\left(k', l', \omega', z, m\right) = \left(f\frac{\partial\left\langle\theta_0\right\rangle(z, x, y)}{\partial z}G_m(z, x, y)\right)^2\Phi_\psi\left(k', l', \omega'\right). \tag{3}$$

Here, $G_m(z, x, y)$ is the $m-$th vertical displacement mode. $\partial\left\langle\theta_0\right\rangle/\partial z$ is the time average local vertical temperature derivative. Eqs. (2, 3) are over-simplified compared to reality. On the other hand, WW14 show that subject to regional adjustment of the various parameters, they are quantitatively useful for a variety of time and space-time series.

The first term on the right in Eq. (2) represents the frequency-wave-number continuum including equal amounts of energy moving both eastward and westward, and northward and southward and is similar to the ZW01 form. The second term on the right represents the asymmetric westward-going energy dominated at low frequencies by the so-called non-dispersive line (NDL) whose slope in $k' - \omega'$ space is controlled by c_x (e.g., WW14). The NDL is conspicuous in altimetric data, in large-part because of its strong barotropic component and by its non-linear coupling to a strongly surface-amplified first baroclinic mode velocity. It is far less prominent in temperatures measured or computed at depth. From the altimetric data, its structure is imposed upon the state estimate at low frequencies and wavenumbers. Whether it is more wave-like or more isolated vortex-like (Chelton et al. 2011) over all frequencies and wavenumbers has not been explored. In either case, when viewed through a low-pass frequency and wavenumber filter, the longest wavelengths and periods are seen. Note that from frequency spectra alone at individual points, one cannot distinguish propagating from standing energy.

When Φ_ψ is integrated over all k', l', the frequency spectrum is obtained (WW14; their Eq. 33):

$$\Omega_\theta\left(\omega'\right) = A\left\{\frac{\pi}{(\alpha-1)L_xL_y}\frac{1}{(1+\omega'^2T^2)} + \frac{\pi}{\sqrt{D}}\exp\left(-L_x^2L_y^2T^2\omega'^2/D\right)\right\}, \tag{4}$$

$$D = c_x^2L_y^2T^2 + L_x^2L_y^2 + c_y^2L_x^2T^2$$

where the second term represents the frequency spectrum of the NDL. Here A absorbs the factor $\left(f\partial\left\langle\theta_0\right\rangle/\partial z\right)^2$. In fitting this frequency form, globally, two changes are made: combined parameters are lumped, and the $1/\left(1+T^2\omega'^2\right)$ term and the NDL term are separated to provide an extra degree of freedom in accounting the known latitudinal composition of Rossby waves. Thus the fit is to:

$$\Omega'_\theta\left(\omega'\right)=\frac{A_1}{(1+\omega'^2T^2)}+A_2\exp(-\omega'^2/P_a) \tag{5}$$

where locally,

$$A_1=\frac{A\pi}{(\alpha-1)\,L_xL_y},A_2=\frac{A\pi}{\sqrt{D}},P_a=\frac{D}{L_x^2L_y^2T^2}, \tag{6}$$

and where the fitting parameters are A_1,T,A_2,P_a. The first term represents a process obeying an ω'^{-2} power law at high frequencies and is intimately related to that of a continuous time AR(1) process (e.g., Hughes and Williams, 2010). Partial derivatives of Eq. (5) show that the value of A_1 depends upon T, etc. The second, exponential, term from the NDL, decays faster in frequency than does any algebraic power. Spectra that are power laws of ω'^{-2} and steeper in some range $\omega'_1\leq\omega'\leq\infty$ are insensitive to aliasing from frequencies above ω'_1 (see Wunsch 1972, Eq. 13; Rhines and Huybers 2011).

A fit was made of $\log\Omega'_\theta\left(\omega',x,y\right))$ to the logarithm of the empirical temperature spectra of ECCOv4 over the range of periods from 20 years to two months. Logarithms are used to render the spectral values more nearly constant with frequency.[1] The resulting parameters vary widely over the global ocean as seen in Figs. 3 - 4.

Overall misfits are generally within about 6% of the state estimate log spectrum relative to the log of the fit spectrum, but not always. Notable features as might have been expected are: (1) Values are spatially noisy, consistent with a comparatively short 20-year time-interval; (2) amplitudes A_1 are small in the tropical oceans with exceptions on eastern boundaries of the Atlantic and Indian Oceans; (3) High latitudes show enhancement of A_1. (4) Over most of the ocean T has values of a few years, with much longer values at high latitudes, and much lower values at low latitudes. More generally, the regions of high values of T are where the spectra tend to be red out to the

[1]Fitting was through a nonlinear trust region method (Seber and Wild 1989, P. 603+; Mathworks Website 2018), a form of least-squares using a search over a variable neighborhood about the most recent estimate.

longest periods. Whether these represent true rednoise processes or the presence of trends has to be examined separately. (5) The contribution of the NDL to temperature is slight almost everywhere. (Exceptions exist to all of these sweeping summaries.) Because of the equivalent spatial complexity and the much smaller amplitudes, the fits to the NDL line are shown in the Appendix. Median values from the fits are $A_1 = 0.070°\mathrm{C}^2/\mathrm{cycle/year}$, T =10.3y, $A_2 = 0.0048°\mathrm{C}^2/\mathrm{cycle/year}$, $P_a = 1.3\mathrm{y}^2$, differing somewhat from the direct fit to the median spectrum (a result expected from a nonlinear estimation process).

An approximate uncertainty of the fitting result can be determined from the inverse Hessian based upon its local value calculated from the Jacobian, which is a by-product of the optimization algorithm (Kalmikov and Heimbach 2014). When multiplied by the covariance matrix of the data noise, it provides an estimate of the uncertainty. The main result is that the 4 parameter estimates have strong and highly variable correlated uncertainties. A global display of the individual 4x4 matrices at each grid point is not easy to digest and is omitted here.

3. Temporal Autocovariance

Oceanic physical processes have a strong frequency dependence, and that leads to the central importance of spectral analyses. On the other hand, for calculating e.g., the expected accuracy of a space or time or space-time average or map, the integrated time-scales included in the covariances are a more convenient tool.

By the Wiener-Khinchin theorem, the temporal autocovariance, $R(\tau)$, and the autocorrelation, $\phi(\tau)$, of the frequency spectrum Eq. (5) are,

$$
\begin{aligned}
R(\tau) &= \frac{1}{2\pi}\int_{-\infty}^{\infty} \Omega'_{\theta}\left(\omega'\right)\cos(\omega'\tau)d\omega' \qquad (7a)\\
&= \frac{1}{\pi}\int_{0}^{\infty}\left[\frac{A_1}{(1+\omega'^2T^2)} + A_2\exp(-\omega'^2/P_a)\right]\cos(2\pi\omega'\tau)d\omega'\\
\phi(\tau) &= R(\tau)/R(0)\\
&= \frac{A_1\pi/(2T)\exp(-\tau/T) + A_2P_a^{1/2}\pi^{1/2}\exp(-P_a\tau^2/4)}{A_1\pi/(2T) + A_2P_a^{1/2}\pi^{1/2}},\ \tau \geq 0
\end{aligned}
$$

Decay time to effective zero correlation $(\phi(\tau_d) = 0.1)$ is shown in Fig. 5 and which can be interpreted as providing the temporal separation required for statistically independent temperature samples at this depth. Tropical areas have times of order one year, while patches (including the central equatorial Pacific) take more than 10 years to decorrelate. This decorrelation time is important in calculations of the accuracy of large-scale sample averages. In low latitudes, samples obtained two years apart could be deemed independent, whereas at high latitudes that can take 10 or more years. The median value is 2.8 years and the mean 3.6 years, omitting values where more than 20 years is required.

4. Wavenumber Spectra

Computation of wavenumber spectral densities involves choosing distances (or areas) over which they are representative, and the presence of complex land boundaries does not lend itself to easy or automatic selection. Here what is done is to separately determine the zonal and meridional wavenumber periodograms along each line of latitude or longitude extending 30° eastward or northward. The calculations are done for each year separately, and then averaged over 20 years to give a power spectrum estimate. Nominal position is assigned to the mid-point longitude or latitude.

Again simplifying the WW14 forms (their Eq. 31) , now omitting the contribution of the NDL which is a pure exponential, the results are then fit to the continuum,

$$\Phi\left(\mathbf{r}_j, k'\right) = B\left(1 + L_y^2 k'^2\right)^{1/2-\alpha} \tag{8}$$

for the zonal spectra, and to

$$\Phi\left(\mathbf{r}_j, l^{prime}\right) = C\left(1 + L_x^2 l^2 l'^2\right)^{1/2-\alpha} \tag{9}$$

for the meridional. Note the pairing of k' with L_y and of l' with L_x, consistent with quasi-geostrophic balance. At high wavenumbers, the behavior is a power law with exponent $1-2\alpha < 0$, if $\alpha > 1/2$, again becoming more white at long wavelengths.

Meridional Wave Numbers

The meridional wavenumber spectrum reflects, in the thermal wind/geostrophic balance, the zonal flows. A large literature exists describing and rationalizing a tendency for the circulation to have preferred zonality, and in the extreme of the appearance of zonal jets (e.g., Chen et al. 2015; Galperin and Reid 2019) . Results of fitting Eq. (9) are displayed in Figs. 6-7. Apart from the prominent western intensification visible in C, both L_x and α are remarkably uniform and stable (α is displayed in the Appendix). Both the mean and median value of $\alpha \approx 3/2$ in contrast to the estimate of $5/2$ by WW14. Year-to-year variations (not shown) do indicate a degree of temporal non-stationarity.

A median spectrum, with best fit of $C = 5.4$, $L_x = 1.2 \times 10^5$km, $\alpha = 1.47$, power law ≈ -2 at high wavenumbers, is shown in Fig. 8. Also shown are the results for a random set of positions. While the amplitude changes considerably, the shape of the spectrum is quite stable. The very large value of L_x is consistent with a long zonal structure in the meridional fluctuations.

The decorrelation distance of the meridional wavenumber spectrum is computed from the cosine transform of Eq. (9). An analytic expression for the autocovariance is,

$$R_l(\xi) = \frac{B\,\xi^{\alpha-2}\,\pi^{\alpha-\frac{1}{2}}\left[\pi\,\xi\,\left(\mathrm{I}_{\alpha+1}\left(\frac{\xi}{\mathrm{L_x}}\right) - \mathrm{I}_{1-\alpha}\left(\frac{\xi}{\mathrm{L_x}}\right)\right) + \mathrm{L_x}\,\alpha\,\mathrm{I}_{\alpha}\left(\frac{\xi}{\mathrm{L_x}}\right)\right]}{(2\,\mathrm{L_x})^{\alpha}\,\Gamma\left(\alpha-\frac{1}{2}\right)\,\sin(\pi\,\alpha)} \tag{10}$$

where I_q is the modified Bessel function. This expression has a straightforward behavior only when $\alpha = m/2$, where m is an integer, and involves subtracting growing exponentials. In practice, a numerical calculation of the cosine transform proves more robust. Generally speaking, the autocovariance of both the median, and from the pointwise calculation at most places, produces a zero correlation at about 750 km. Beyond that distance, the autocovariance often becomes strongly negative.

Zonal Wavenumber Spectra

Zonal wavenumbers reflect the meridional quasi-geostrophic variability structure. Zonal flow dominance at long periods suggests, a priori, that the zonal wavenumbers may be much noisier (unstable) than the meridional ones. Results for the zonal structure parameters are shown in Figs. 9-11 and the instability of results is manifested in the complex spatial variations in C in Fig. 9. Analyzed zonal arc length varies with latitude from about 2000 to 3300 km. As with the meridional wavenumber values, the zonal wavenumber periodograms were computed for each location and each year and then averaged over the 20 years, thus suppressing the year-to-year variability. Parameter values (from fitting the median spectrum) are: $B = 63$, $L_y = 7910$ km, $\alpha = 1.6 \approx 3/2$, power law, ≈ -2, again.

With the different results for zonal and meridional spectra, any wavenumber isotropy assumption must be examined carefully and is surely different for time scales associated with internal waves and balanced and sub-mesoscale eddies than it is for the general circulation scales dominating the results here.

5. Vertical Structure

With some exceptions (e.g., Blumenthal and Briscoe 1995; Polzin and Lvov 2011) the internal wave band can be represented with vertically propagating free waves—that is without vertical modal structure. In contrast (Wunsch 1997, Arbic et al. 2014, Hochet et al. 2015, Lacasce 2017), the balanced eddy field band appears to be dominated by the barotropic and first baroclinic modes with higher modes being much weaker. The often-observed coupling of these two lowest modes (Wunsch 1997, Wang et al. 2013, Lacasce 2017, and others) is rationalized as the tendency of topographic features to minimize the horizontal velocity at and near the bottom over topography. These inferences rely heavily on the in situ current meter measurements that have been accumulated over the last several decades, and with some indirect inferences made from the altimeter data. The longest in situ records do not generally surpass two years in length, and their geographical distribution remains sparse and irregular. [2]

Absence of long duration moored data means that little or nothing is known about the full vertical structure of temperature variability over years and decades apart from some regional inferences (e.g., Bindoff and McDougall, 1994) based upon the temporally sparse deep CTD data. In an initial reconnaissance, the ECCOv4 state estimate/climatology will be used to describe the vertical structures extending out to 20 years. How is that best done?

In the context of the balanced eddy band the moored data, where available, produced a reasonably efficient representation in terms of the linear, *flat bottom,* modes (which are a complete set). Such a representation has the virtue of being consistent with the horizontal Fourier frequency/-wavenumber representations of WW14. On the other hand, the inference of very strong topographic effects, and the known complexities in the time and space scales (e.g., Wunsch 2015; Lacasce 2017) of vertical and horizontal propagation of linearized $\beta-$dominated motions make

[2] The isolated Bermuda Station S and the Hawaiian HOT series are exceptions albeit subject to temporal aliasing problems.

any such choice seem arbitrary. Consider the differences between linear baroclinic wave propagation in the equatorial regions, at mid-latitudes, and at high-latitudes. Response e.g., in the Rossby wave regime, to eastward going forcing disturbances produces vertically trapped ("negative equivalent depth") solutions, while westward moving forcing radiates wave-like motions into the deep interior. Varying topographic slopes will have very different effects on energy that does reach the bottom topography, and the influences of mean flows are very important, particularly at high latitudes.

In the spirit of exploration, we instead here use the singular value decomposition (empirical orthogonal functions, or EOFs, and several other terminologies). Consider the temperature anomaly field, written as a matrix for $\theta\left(\mathbf{r}_j, z_m, t_n\right)$ at horizontal position $\mathbf{r}_j$, at vertical positions z_m, and times (years t_n; only yearly averages are being used for this purpose). With $\mathbf{r}_j$ fixed, the Eckart-Young-Mirsky Theorem shows that a *perfect* representation by the singular value decomposition (SVD) is,

$$\theta\left(\mathbf{r}_j, z_m, t_n\right) = \mathbf{U}\Lambda\mathbf{V}^T = \sum_{j=1}^{L} \lambda_j\left(\mathbf{r}_j\right)\mathbf{u}_j\left(\mathbf{r}_j, z_m\right)\mathbf{v}_j^T\left(\mathbf{r}_j, t_q\right), \text{fixed } \mathbf{r}_j \tag{11}$$

where the orthonormal columns, $\mathbf{u}_j\left(z_m\right)$, of $\mathbf{U}$ carry the vertical structure and are often known as the EOFs. Arguments z_m and t_q have been written on the right side of Eq. (11), for mnemonic reasons. Each $\mathbf{u}_j$ has length equal to the number of local depths being used, and the number of columns, L, in $\mathbf{U}$, is less than or equal to the smaller of the number of depths, z_m and the number of years, here 20. Thus L never exceeds 20. The orthonormal columns, $\mathbf{v}_m$, of matrix $\mathbf{V}$ each carries the time representation of the corresponding $\mathbf{u}_m$. Their length is the number of years. Diagonal matrix Λ has elements λ_j known as the singular values. $\mathbf{u}_j, \mathbf{v}_j$ are the singular vectors. (See Lawson and Hansen 1995 or Wunsch 2006; Λ is not usually square, but a main diagonal is still defined in the obvious way.) Dimensions are most conveniently associated with λ_j, the vectors being dimensionless.

This representation is particularly useful when the *effective* number of singular values/vectors is very small compared to the maximum number possible. If Eq. (11) is truncated at a value $K \leq L$, the fraction of the variance in $\boldsymbol{\theta}$ that is captured by the representation is,

$$F(K) = \frac{\sum_{j=1}^{K} \lambda_j^2}{\sum_{j=1}^{L} \lambda_j^2} \leq 1,\ K \leq L \tag{12}$$

If a useful value of K is much less than L, e.g., 1 or 2, a concise description is available of an otherwise potentially very complex field. A corollary of the Eckart-Young-Mirsky Theorem is that no other pair of K-orthogonal vectors can increase the captured variance. In what follows, the vertical and temporal structure of the annual mean temperatures in the state estimate are explored, with a focus on those regions where a very small number (i.e., $K = 1$ or 2) captures the structure of interannual variability.

A priori, the barotropic mode, if it exists, is not expected to make a measurable contribution to temperature variability. The variance of temperature is such a strong function of depth that fitting temperature directly produces results dominated by the upper ocean. For numerical accuracy, $\theta(\mathbf{r}_h, z)$ is first weighted by dividing the temperature anomaly by the *local* time average full vertical temperature profile, $\partial \langle \theta_0 \rangle / \partial z$, as determined from the state estimate:

$$G(\mathbf{r}, z_j, t) = \frac{\theta(\mathbf{r}_j, z_m, t_q)}{\partial \langle \theta_0(\mathbf{r}_j, z_m) \rangle / \partial z} \tag{13}$$

The SVD is thus being applied to a weighted temperature, rendering the units of the singular values as meters. Because $\partial \langle \theta_0 \rangle / \partial z$ is itself noisy, the effect of the division in Eq. (13) is to make the displacement even noisier. Experiments were conducted by using instead the global median value of $\partial \langle \theta_0 \rangle / \partial z$, but although it produced a somewhat smoother result, the variability in the mean profile is sufficiently great spatially that use of a fixed form can distort the results. G should *not* be interpreted as a vertical displacement, as that requires the validity of the local equation,

$$\frac{\partial \theta}{\partial t} + w\frac{\partial \theta}{\partial z} = 0 \tag{14}$$

which has no contribution from diffusion or from lateral advection, $\mathbf{u}_h \nabla_h \theta$. Both processes are important at periods of years and longer. G is best interpreted simply as a vertically weighted temperature anomaly.[3] The vertical structure of temperature itself is recovered by multiplying back $\mathbf{u}_j\left(\mathbf{r}_j, z_m\right) \partial \left\langle \theta_0 \left(\mathbf{r}_j, z_m\right)\right\rangle / \partial z$, re-weighting to the upper ocean. The only drawback compared to applying the SVD to unweighted temperatures is that these re-weighted $\mathbf{u}_j$ are not mutually orthonormal. Fits here are made between 105m depth, and 3900m depth or the bottom, whichever is shallower. Unlike the balanced eddy band, the only qualitative generalization is that the result is spatially complex. Examples along two longitudes are shown in Fig. 12. Regions where the lowest singular vector, $\mathbf{u}_1(z)$, contain 90% or more of the variance (Fig. 13) appear to be restricted largely to the South Atlantic and Indian Oceans. Use of the first two $\mathbf{u}_i$ results in a much greater coverage (Fig. 14), although the corresponding vertical structures in $\mathbf{v}_i$ are very diverse. Any relationship to the linear flat bottom modes, or e.g., the "surface modes" of Lacasce (2017) and others, and their relevance at these much longer periods, remains to be explored.

The conventional flat bottom baroclinic vertical displacement mode number is the number of zero-crossings plus one (Fig. 15). Thus the first baroclinic mode represents a unidirectional movement of the whole water column up or down and the 2nd vertical mode has one zero crossing at

[3] A global test (not shown) of the time-average "abyssal recipes" point balance of $w\partial < \theta_0 > /\partial z = k\partial^2 < \theta_0 > /\partial z^2$ showed only extremely limited regions of useful accuracy, even in regions of relatively flat time-mean isopycnals. Terms such as $u\partial < \theta_0 > /\partial x$ are important and that is likely also true of the time-dependent balances. Liang et al. 2017) discuss the complexity of the calculated w field, and the importance of the bolus contribution.

depth.[4] A unidirectional mode (no zero crossings) does dominate much of the Pacific and Indian Oceans, but with considerable regions having a sign reversal with depth. One might have hoped that the $\mathbf{u}_i$ would reflect local linear dynamical modes, but given the general inaccuracy of Eq. (14), any such interpretation should be resisted. Instead, a complicated vertical structure emerges even where one singular vector is dominant, particularly in the South Atlantic and northern Indian Oceans.

Although not shown here, the same calculation using the unweighted temperature anomalies has a similar vertical complexity, although the magnitudes in the abyssal ocean are much smaller, as expected, and with deep reversals with depth.

6. Temporal Trends

Each vertical orthonormal singular vector $\mathbf{u}_i$ is accompanied by a time-varying orthonormal vector $\mathbf{v}_i$. The temporal variations of the lowest, singular vector, $\mathbf{u}_1$ often exhibit a visual trend over the duration of the state estimate. The significance of these trends, in the presence of a general rednoise in the variability, the known long memory in the ocean, and concerns about residual model drifts make it not easy to evaluate. Model drift is however, suppressed by the use of data sets spanning the whole time domain.

Ultimately, a breakdown of the $\mathbf{v}_i$ by frequency band is sought. But given the brief 20-year interval available, only the time-domain structures are described. By fitting a least-squares straight line to each $\mathbf{v}_{1,}$ about 80% of the results are significant at two-standard deviations (determined from the fit itself; Fig. 16) and a near-Gaussian distribution. A number (far from all) of the $\mathbf{v}_1$ visually depict a quasi-linear trend (e.g., Fig. 12). Of those, despite the largest value at the

[4]This description is incomplete in the sense that very close to the sea surface, another reversal of sign occurs, one providing movement of the free surface to compensate the upper ocean thermally derived pressure field. (See Wunsch 2013). By starting the fits below 100 meters, this structure is unseen by the SVD analysis.

maximum positive slope, slightly more than half the significant slopes are negative, but the net heating or cooling can be calculated only from the full water column (see references in Fukumori et al. 2018). Regions of positive and negative slope are shown in Fig. 16.

Some of the intricate structure of trends and depth dependence can be seen in Fig. 12. In the Atlantic, the temporal change at all but the highest latitude shown (42°N) is a nearly monotonic trend (warming). That warming corresponds to those depths where the corresponding $\mathbf{u}_1$ is positive, but would be a cooling where $\mathbf{u}_1$ is negative.

In the east central Pacific Ocean, a cooling trend is visible at 21°N, predominantly at the bottom—consistent with existing analyses showing deep North Pacific cooling (Fukumori et al. 2018; Gebbie and Huybers 2019). At 30°S $\mathbf{v}_1$ is nearly unchanged until about 2008 when a warming over almost the whole water column sets in. Near the equator (0.6°N), a maximum at the time of the 1997-1998 El Niño is visible and is a general feature of the near equatorial Pacific Ocean.

7. Other Condensed Descriptors

The central difficulty encountered in this description is the apparent need for a localized frequency/wavenumber/covariance decomposition at every point with the volume of numbers becoming indigestible. One possible condensation is given by the decorrelation times or distances discussed above. Other summary numbers, useful for model comparisons, etc. do exist: for example, the spectral moments. Consider e.g., the frequency moments. Vanmarcke (1983) defines the "characteristic frequency of the spectral moments" μ_k of a power density spectral estimate, $\Phi(\omega')$,

$$\mu_k = \left[\frac{\int_0^{\omega'_{\max}} \Phi(\omega')\, \omega'^k d\omega'}{\int_0^{\omega'_{\max}} \Phi(\omega')\, d\omega'} \right]^{1/k}, \; \omega'_{\max} = 1/(2\Delta t). \tag{15}$$

These have dimensions of a frequency. Of particular importance are $\mu_{1,}\mu_2$ which can be interpreted as the mean frequency, and the root-mean square frequency. Another useful summary number is the "spectral bandwidth" (Vanmarcke, 1983) $\varepsilon = (1-\mu_2/\mu_4)^{1/2}$. Fig. 17 shows the calculated value of the period $1/\sqrt{\mu_2}$ from numerically summing the frequency spectrum derived from the *annual mean* values. A useful physical interpretation is (Vanmarcke 1983, Eq. 4.4.6) that the expected rate of zero-crossings of the temperature anomaly at each point is just $\sqrt{\mu_2}$ and thus $1/\sqrt{\mu_2}$ is an estimate of the interval between sign changes in the temperature anomaly through time. See Wunsch and Heimbach (2013) for oceanographic application to the occurrence of extreme events and other properties. The calculated range here is roughly by a factor of two, with a general, if not consistent, tendency for low latitudes to have shorter intervals than higher latitudes and a complicated behavior near the western boundary currents.

8. Summary and Discussion

Results here are a tentative description of low frequency variability, subject to the numerous assumptions made throughout, and are a mixed bag. The "why" has to be taken up separately. To a great extent, the best qualitative global description is the characteristic complexity itself. On the other hand, a simplified form of the Wortham and Wunsch 2014; WW14) temporal frequency spectral form does succeed in describing with useful accuracy much of the near-global temperature variability in the ECCOv4 state estimate. Dominant zonality of oceanic low-frequency variability emerges in the spatial stability/instability of the meridional/zonal wavenumber spectra. Vertical structure corresponding to the lumped variability at periods lying between 1 and 20 years proves to be complex, vertically, horizontally, (and temporally), and without any obvious globally dominant physics. The problem appears to be somewhat like that faced by geologists: in that field, every location has a nearly unique, noisy stratigraphy and geochemistry, but regional syntheses exist, and a few principles (those of plate tectonics, volcanism, mountain building, sedimentation, etc.) can be perceived as acting globally with widely varying importance.

With the numerous long time-scales of adjustment/memory in the ocean, and the complicated, effectively permanent, topographic features, that a 20-year interval produces a very complex pattern of variability is not surprising. Oceanic bottom topography does influence the whole water column–which becomes clearer as near-surface higher frequency structures are suppressed by averaging—and is a very complicated, spatially non-stationary, anisotropic, two-dimensional permanent disturbance. Over long time scales, the variety of atmospheric variations in space and time, in wind, precipitation, evaporation, and temperature, also affect the underlying ocean in geographically complicated ways, including oceanic flow redistribution effects.

In contrast with much variability in nature generally, the structure of the higher frequencies (the balanced eddies and the internal wave band) is simpler here than in the lower frequencies. What remains imponderable is whether e.g., a 200 year duration would produce a simpler pattern of time mean and variability? Some insight into the 100 year and longer changes in the ocean can be found in Roemmich et al. (2012) and Gebbie and Huybers (2019).

The reader is reminded that these results all rest on the accuracy of the least-squares-fitted ECCOv4 version of the MITgcm. In particular, apart from temporally and spatially sparse CTD casts, direct measurements of the lower 50 percent of water column temperature variability over recent years and decades are lacking. Inferences here rest upon the ability of the dynamical equations to combine the diverse altimetric, Argo, meteorological, and other data to infer the full water column physics. Extended-duration full-water-column measurements would be useful as tests of system skill.

Another important question is whether better methods exist to depict the spatially and temporally changing character of oceanic variability? The appeal and power of Fourier representations is clear, but the non-stationary character of the fields renders awkward conventional results—particularly those applying to the wavenumber domain. Alternatives do exist. Wunsch and Stammer 1995) produced a global description of altimetric variability using spherical harmonics. Adaptive methods, perhaps based upon empirical mode decompositions (Huang et al. 1998) or Slepian functions (Simons et al. 2006) or cluster analysis or some combination need also to be explored.

(All of the fields discussed here are available in Matlab form on request to the author and all ECCO fields are publicly accessible through the Jet Propulsion Laboratory.)

Acknowledgments. Funded in part from the Jet Propulsion Laboratory, NASA Contract NNN12AA01C with MIT. I had very useful comments from Brian Arbic, Joe Lacasce, Raf Ferrari, Joern Callies and two helpful anonymous referees. Thanks to all the members of the ECCO Consortium and the originators of the data who made this work possible.

APPENDIX

This Appendix includes some additional charts showing the results of the analytic fits to the estimated frequency and wavenumber fields. For the frequency spectra, Figs. A1, A2 show the amplitude and exponential scale factor of the non-dispersive line (NDL). Amplitudes are generally considerably weaker then in the continuum term. Also shown (Figs. A3, A4) are the exponents α for the meridional and zonal wavenumber spectra and which prove relatively featureless.

Abernathey, R. and C. Wortham 2015: Phase speed cross spectra of eddy heat fluxes in the eastern Pacific. J. Phys. Oc. 45, 1285-1301.

Arbic, B. K., Scott, R.B., Flierl, G. R., Morten, A. J., Richman, J G., Shriver, J. F. 2012: Nonlinear cascades of surface oceanic geostrophic kinetic energy in the frequency domain. J. Phys. Oc. 42, 1577-1600.

Arbic, B. K., M. Muller, J. G. Richman, J. F. Shriver, A. J. Morten, R. B. Scott, G. Serazin and T. Penduff 2014: Geostrophic turbulence in the frequency-wavenumber domain: eddy-driven low-frequency variability. J. Phys. Oc. 44, 2050-2069.

Bindoff, N. L. and T. J. McDougall 1994: Diagnosing climate change and ocean ventilation using hydrographic data. J. Phys. Oc., 24, 1137-1152.

Blumenthal, M. B. and M. G. Briscoe 1995: Distinguishing propagating waves and standing modes: an internal wave model. J. Phys. Oc. 25, 1095-1115.

Callies, J. and W. Wu 2019: Some expectations for submesoscale sea surface height variance spectra. J. Phys. Oc., J. Phys. Oc., submitted.

Chelton, D. B., Schlax, M. G.,Samelson 2011: Global observations of nonlinear mesoscale eddies. Prog. Oceanog., 91, 167-216.

Chen, R., G. R. Flierl and C. Wunsch 2015: Quantifying and interpreting striations in a subtropical gyre: a spectral perspective. J. Phys. Oc. 45: 387-406.

Fukumori, I., P. Heimbach, R. M. Ponte and C. Wunsch 2018: A dynamically-consistent ocean climatology and its temporal variations. Bull. Am. Met. Soc., 2107-2128.

Gebbie, G. and P. Huybers 2019: The Little Ice Age and 20th-century deep Pacific cooling. Science 363(6422): 70+.

Hochet, A., A. C. de Verdiere and R. Scott 2015: The vertical structure of large-scale unsteady currents. J. Phys. Oc. 45, 755-777.

Huang, N. E., Z. Shen, S. R. Long, M. L. C. Wu, H. H. Shih, Q. N. Zheng, N. C. Yen, C. C. Tung and H. H. Liu 1998: The empirical mode decomposition and the Hilbert spectrum for nonlinear and non-stationary time series analysis .Proc. Roy. Soc. A, 454, 903-995

Hughes, C. W. and S. D. P. Williams 2010: The color of sea level: Importance of spatial variations in spectral shape for assessing the significance of trends. J. Geophys. Res.-Oceans 115.

Hughes, C. W., J. Williams, A. Blaker, A. Coward and V. Stepanov 2018: A window on the deep ocean: The special value of ocean bottom pressure for monitoring the large-scale, deep-ocean circulation. Prog. Oceanog 161, 19-46.

Kalmikov, A. and P. Heimbach 2014: A Hessian-based method for uncertainty quantification in global ocean state estimation.Siam Journal on Scientific Computing 36, S267-S295.

Komen, G. J., L. Cavaleri, M. A. Donelan, K. Hasselmann, S. Hasselman and P. A. E. M. Janssen 1994: Dynamics and Modelling of Ocean Waves. Cambridge ; New York, NY, USA, Cambridge University Press.

LaCasce, J. H. 2017: The prevalence of oceanic surface modes. Geophys. Resd. Letts. 44, 11097-11105.

Lawson, C. L. and R. J. Hanson 1995: Solving Least Squares Problems, SIAM, Philadelphia.

Liang, X., M. Spall and C. Wunsch 2017: Global ocean vertical velocity from a dynamically consistent ocean state estimate. J. Geophys. Res. 122, 8208-8224.

Marshall, J., C. Hill, L. Perelman and A. Adcroft 1997: Hydrostatic, quasi-hydrostatic and non-hydrostatic modelling. J. Geophys. Res., 102, 5733-5752.

Munk, W. 1981: Internal waves and small-scale processes. in Evolution of Physical Oceanography. Scientific Surveys in Honor of Henry Stommel. B. A. Warren and C. Wunsch, The MIT Press, Cambridge, Ma (also at http://ocw.mit.edu/ans7870/resources/Wunsch/wunschtext.htm): 264-291.

Penduff, T., M. Juza, L. Brodeau, G. Smith, B. Barnier, J.-M. Molines, A.-M. Tréguier and G. Madec 2010: Impact of global ocean model resolution on sea-level variability with emphasis on interannual time scales. Oc. Sci. 6, 269-284.

Polzin, K. L. and Y. V. Lvov 2011: Toward regional characterizations of the oceanic internal wavefield. Revs. Geophys. 49.

Rhines, A. and P. Huybers 2011: Estimation of spectral power laws in time uncertain series of data with application to the Greenland Ice Sheet Project 2 delta O-18 record. J. Geophys. Res.-Atmospheres 116.

Roemmich, D., W. J. Gould and J. Gilson 2012: 135 years of global ocean warming between the Challenger expedition and the Argo Programme. Nature Clim. Change 2, 425-428.

Samelson, R. M., M. G. Schlax and D. B. Chelton 2016: A linear stochastic field model of midlatitude mesoscale variability. J. Phys. Oc. 46, 3103-3120.

Scott, R. B., B. K. Arbic, E. P. Chassignet, A. C. Coward, M. Maltrud, W. J. Merryfield, A. Srinivasan and A. Varghese 2010: Total kinetic energy in four global eddying ocean circulation models and over 5000 current meter records. Ocean Model. 32, 157-169.

Simons, F. J., F. A. Dahlen, M. A. Wieczorek 2006: Spatiospectral localization on a sphere. SIAM Rev., 48, 504-536.

Sonnewald, M., C. Wunsch and P. Heimbach 2019: Unsupervised learning reveals geography of global ocean dynamical regions Earth and Space Science, 6. https://doi.org/10.1029/2018EA000519.

Vallis, G. K. 2017: Atmospheric and Oceanic Fluid Dynamics: Fundamentals and Large-Scale Circulation. Cambridge UK, Cambridge Un. Press.

Wang, J., G. R. Flierl, J. H. LaCasce, J. L. McClean and A. Mahadevan 2013: Reconstructing the ocean's interior from surface data. J. Phys. Oc. 43, 1611-1626.

Wortham, C. and C. Wunsch 2014: A multi-dimensional spectral description of ocean variability. J. Phys. Oc. 44, 944-966.

Wunsch, C. 1972: Bermuda sea level in relation to tides, weather, and baroclinic fluctuations. Revs. Geophys. 10: 1-49.

Wunsch, C. 1997: The vertical partition of oceanic horizontal kinetic energy. J. Phys. Oc. 27, 1770-1794.

Wunsch, C. 2006: Discrete Inverse and State Estimation Problems: With Geophysical Fluid Applications. Cambridge ; New York, Cambridge University Press.

Wunsch, C. 2013: Baroclinic motions and energetics as measured by altimeters. J. Atm. Ocean. Tech. 30, 140-150.

Wunsch, C. 2015: Modern Observational Physical Oceanography, Princeton Un. Press.

Wunsch C. 2019) How accurate are ocean mean temperature estimates? To be published.

Wunsch, C. and P. Heimbach 2013: Two decades of the Atlantic meridional overturning circulation: anatomy, variations, extremes, prediction, and overcoming its limitations. J. Clim. 26, : 7167-7186.

Xu, Y. S. and L. L. Fu 2012: The effects of altimeter instrument noise on the estimation of the wavenumber spectrum of sea surface height. J. Phys. Oc. 42, 2229-2233.

Zang, X. and C. Wunsch 2001:. Spectral description of low frequency oceanic variability. J. Phys. Oc., 31, 3073-3095.

LIST OF FIGURES

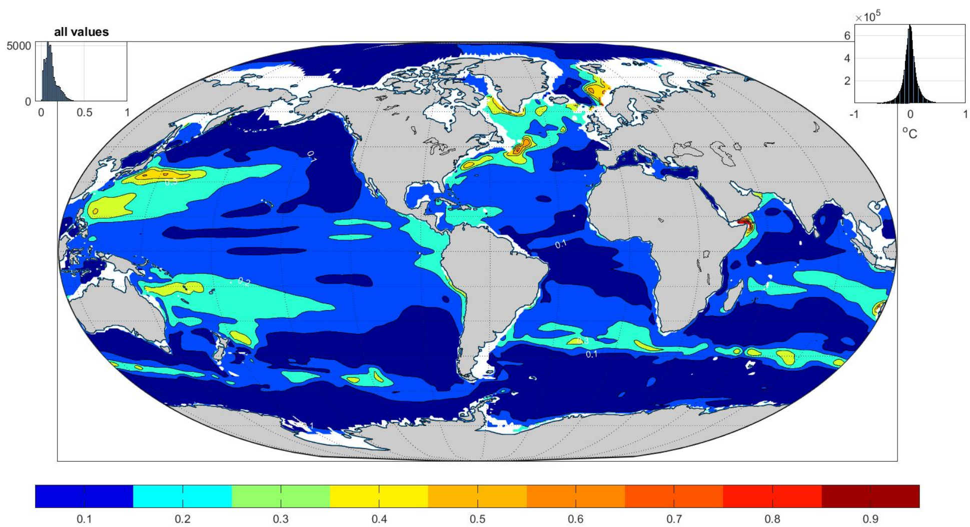

FIG. 1. Standard deviation (^oC) from monthly anomalies of the temperature at 477m. Upper left inset is the distribution of standard deviations, and upper right shows the distribution of underlying temperature anomalies over all points and times and its unimodal character. The mean value is 0.12 and the median 0.10 ^{o} C.

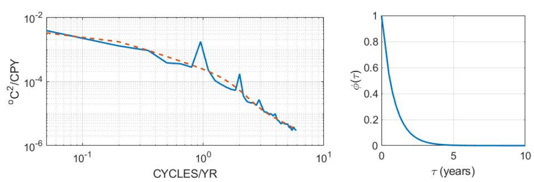

FIG. 2. Median spectral density estimate, $^o\,C^2$/cpy, from all those computed of the monthly mean temperatures at 477m in the state estimate (solid line). Frequency, ω' is cycles/year. Dashed line is the fit of the analytic spectrum to the median. Note the prominent annual, semi-annual and higher harmonic peaks which are included in the overall fits. Direct fits to the median spectrum produce $A_1 = 0.058^0\mathrm{C}^2/cpy, T = 8.1\mathrm{y}$, $A_2 = 0.003^o\mathrm{C}^2/cpy, P_a = 1.6\mathrm{y}^2$. The decorrelation times and distances discussed in the text would enter into a formal calculation of the confidence limits on this result. The 95% confidence limit is approximated by about the small excursion limits in the high frequency range.

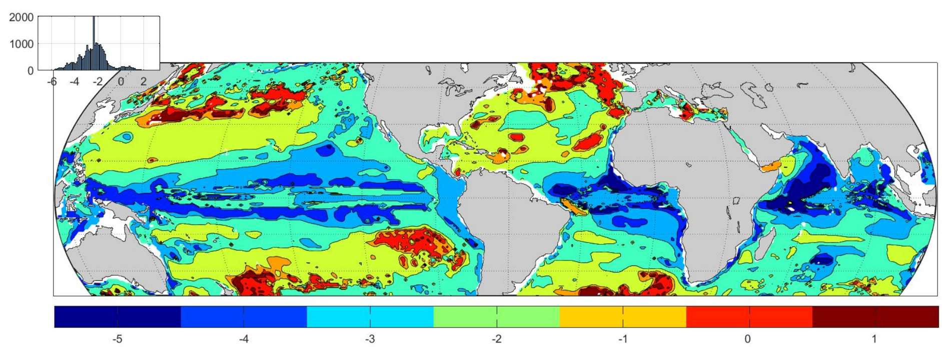

FIG. 3. $\log_{10}(A_1)$, where A_1, ^{o} C ^{2}/cpy, is the fitted coefficient. A tendency for small values in the tropics and high values at higher latitudes is evident, albeit with a considerable zonal structure. Compare to Fig. 1 showing that A_1 is not simply an amplitude, but that the total power is controlled also by T.

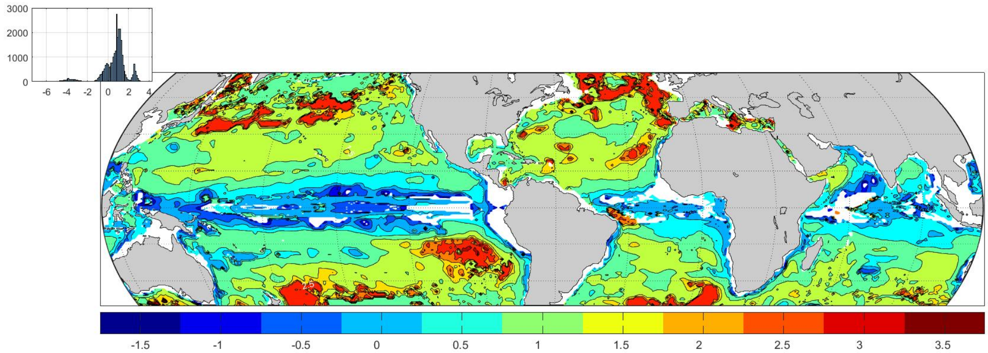

638 FIG. 4. $\log_{10}(T)$ years where T is from the nonlinear least-squares fit. A strong spatial correlation with A_1 is evident consistent with the behavior of the inverse Hessian (not shown) Note the multi-modal behavior.

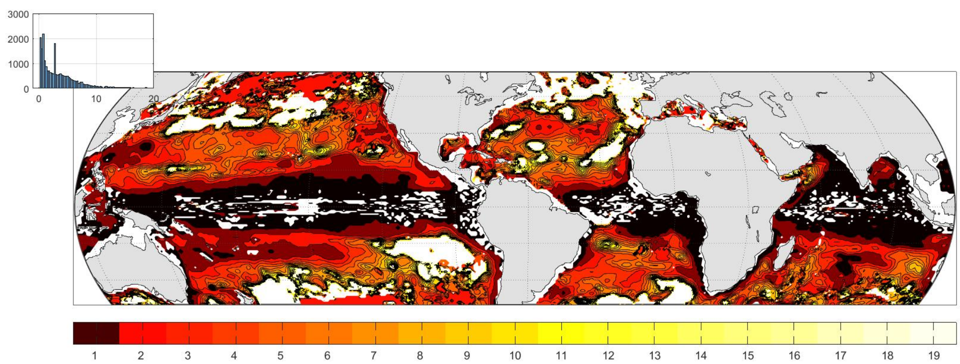

FIG. 5. Time in years τ_d for the magnitude of the temporal autocorrelation to fall to 0.1. In white areas, the correlation never becomes as small as 0.1. Based on the both the continuum ω'^2 and NDL terms in the analytic form in Eq. (7a).

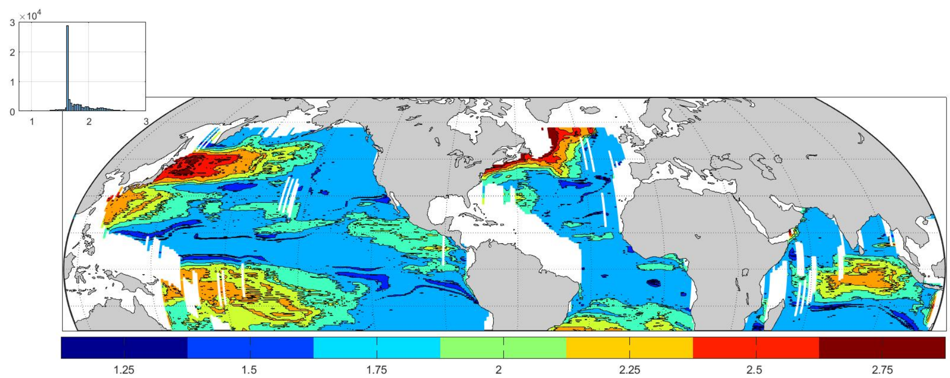

FIG. 6. $\log 10(C)$, ^{o} C^2/cpy, in the meridional wavenumber spectral density (Eq. 9). Both visually and in the histogram, a considerable fraction of the ocean has a nearly uniform value, albeit the western boundary areas are distinctly stronger. Values are assigned to the mid-points of vertical strips of 30 degrees of latitude and white areas are within 15 degrees of the coast. Isolated white stripes result from island presence in the strip.

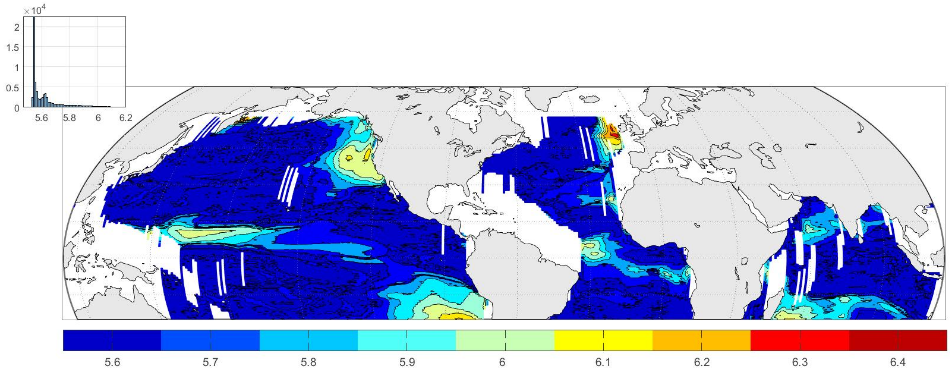

FIG. 7. The nearly uniform open ocean value of $\log_{10}(L_x)$ in the meridional wavenumber spectrum. Here eastern boundaries tend to stand out. Median value is about 380km. Mean is about 460km.

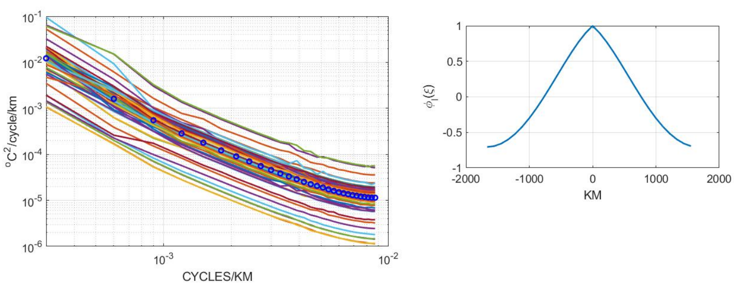

FIG. 8. (left panel). Median meridional wavenumber spectrum ('o', not the fit) and wavenumber spectra from a random selection of positions. (right panel) Autocorrelation corresponds to the median meridional wavenumber spectrum and is typical of most of the ocean. The spectrum remains reddish at long wavelengths..

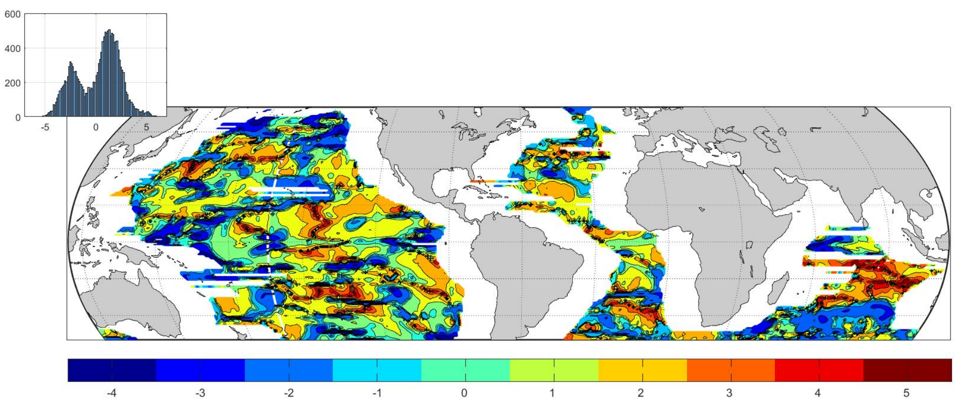

FIG. 9. $\log_{10}(B)$, ^{o} C ^{2}/cpy, in the zonal wavenumber spectral density. Note that the 30° choice of zonal extent precludes values extending westward more than 30° from the coastline. Values are assigned to the mid-point position in longitude. In a quasi-geostrophic system, zonal wavenumbers reflect the meridional flow field. The result is bimodal.

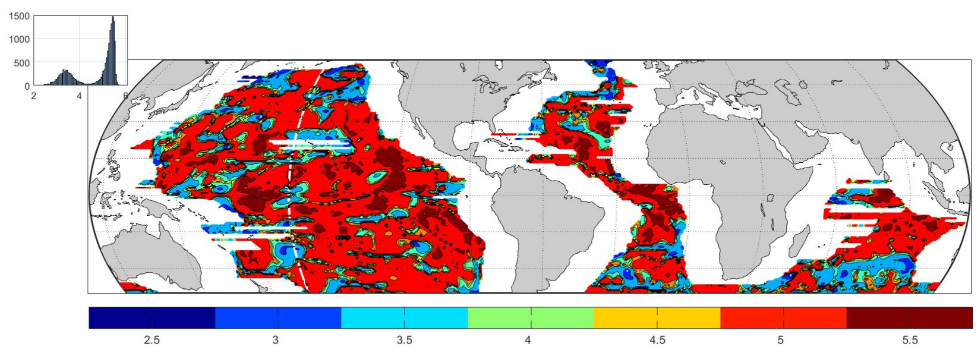

FIG. 10. $\log_{10}, L_y$ in kms, in the zonal wavenumber spectral estimates. Strong bimodality again appears.

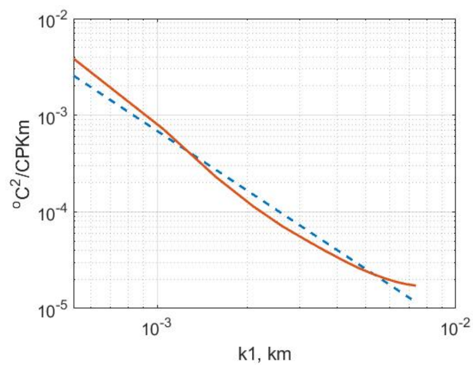

FIG. 11. Median zonal wave number spectral density and the corresponding fit (dashed line).

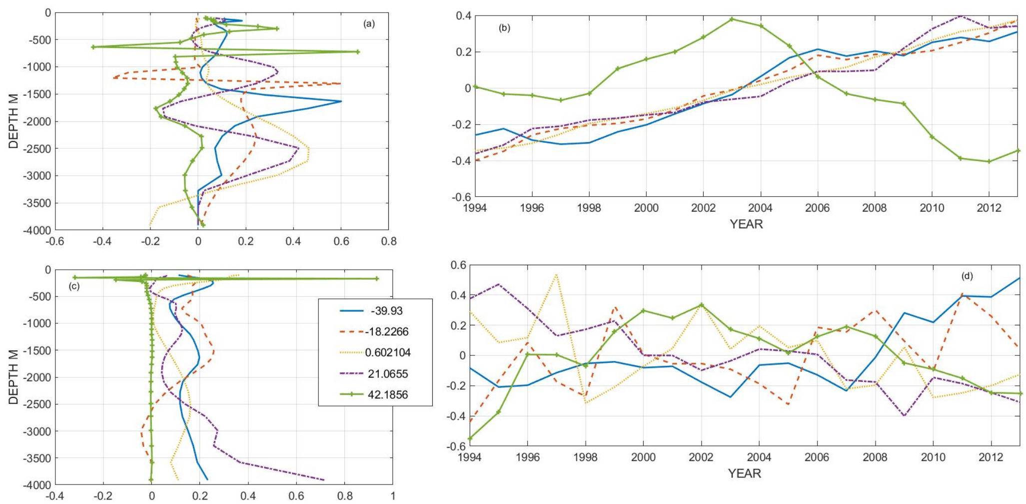

FIG. 12. Pairs of $\mathbf{u}_1(a), \mathbf{v}_1$ (b) along the meridian 10°W in the Atlantic Ocean at every 25th meridional grid point. Linear trends are visually present, with the strong exception at 42°N, where the initial years imply cooling (increase of negative values of $\mathbf{u}_1$) and warming after about 2004. (c,d) Same as (a,b) except along longitude 150°W in the Pacific Ocean. Linear trends are not obvious and note the strong bottom intensification at 21°N of a slight cooling.

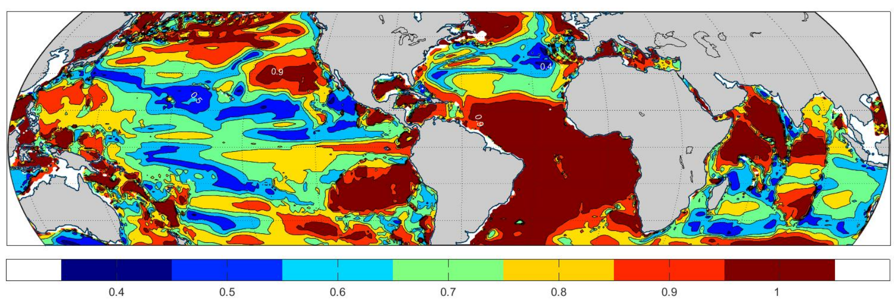

FIG. 13. Fraction of the variance lying in the first singular vector (EOF) of vertically weighted temperature through depth and time (years). Regions where the value exceeds 0.9 are largely limited to the South Atlantic and the western Indian Ocean. In general the Atlantic is simpler in this special sense than is the Pacific, but the structures of $\mathbf{u}_1$ are very variable within those areas.

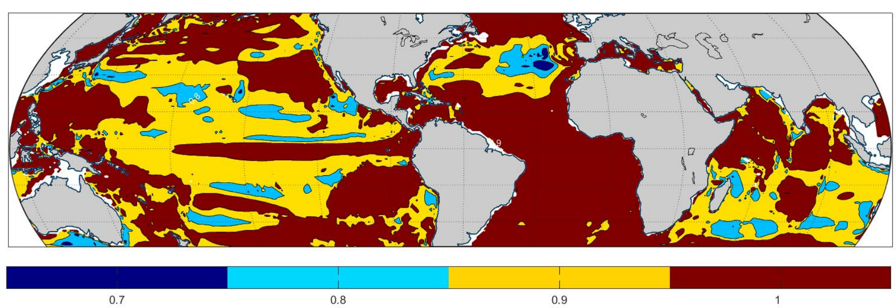

FIG. 14. Fraction of the variance included in the first *two* $\mathbf{u}_i$ singular vectors. Most of the ocean exceeds 90%.

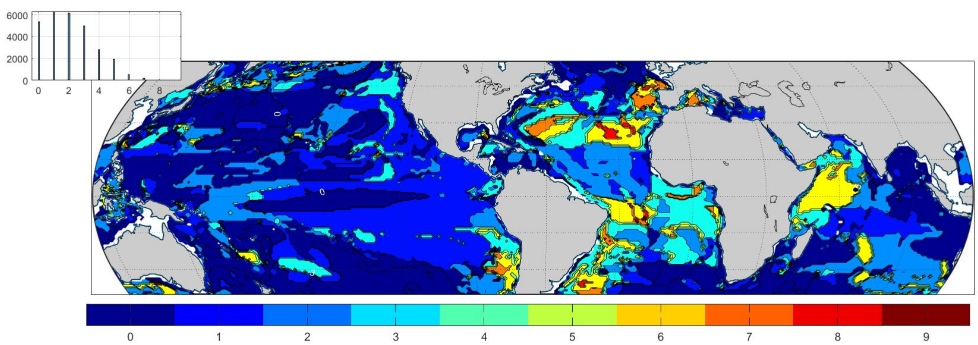

FIG. 15. Number of zero crossings, n_z, in the vertical in the first singular vector $\mathbf{u}_1$) for temperature in depth/time. In conventional mode terms, the baroclinic mode number is $n_z + 1$. Regions roughly similar to a simple first baroclinic mode ($n_z = 0$, possibly representing a unidirectional vertical displacement) are unusual. More common are regions resembling a mode 2 dominance with a zero-crossing in the vertical.

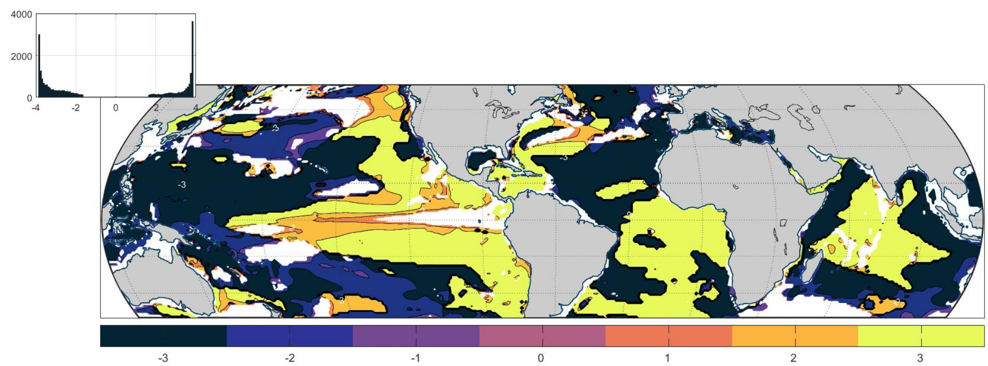

FIG. 16. Values of $100\times$ the linear slope in $\mathbf{v}_1$ where it exceeds 2 standard deviations of the fit error. *The slope pertains to the value of the maximum of* $\mathbf{u}_1$, defined as always positive. Thus a negative value here means that the depth of maximum change is cooling in the 20 year average. Whether the rest of the water column is cooling or warming depends upon the number of zeros in $\mathbf{u}_1$. Some locations show no trend of either sign (white areas).

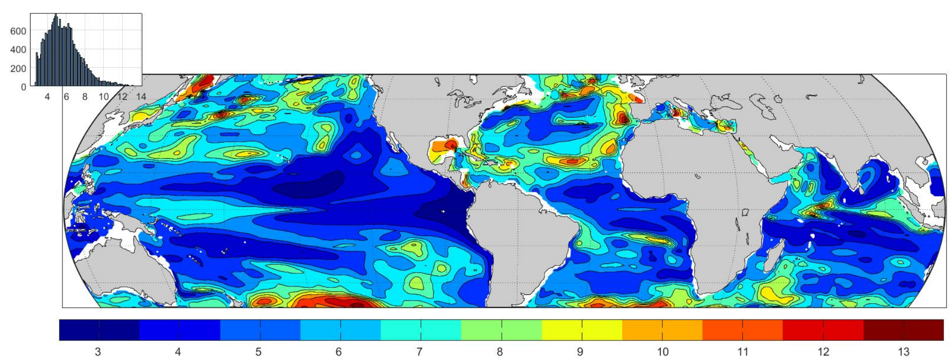

674 FIG. 17. Time scale (years) associated with the second moment of the frequency periodogram at each grid point at 477m annual average values.

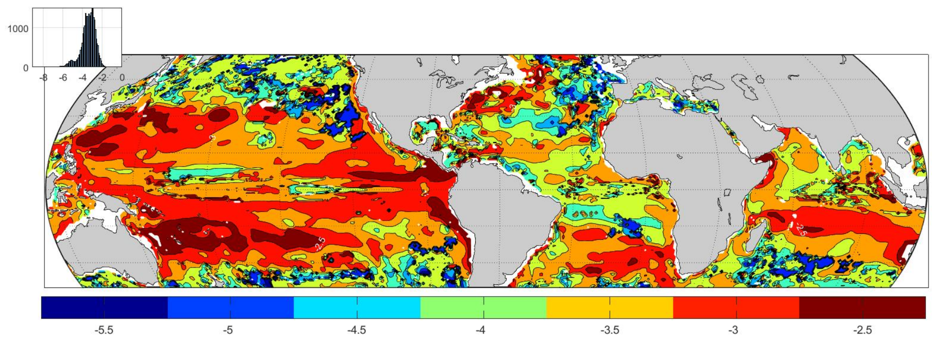

Fig. A1. log(A_2), ^{o} C/cpy, the coefficient of the nondispersive line frequency contribution. A_2 is generally an order of magnitude smaller than A_1.

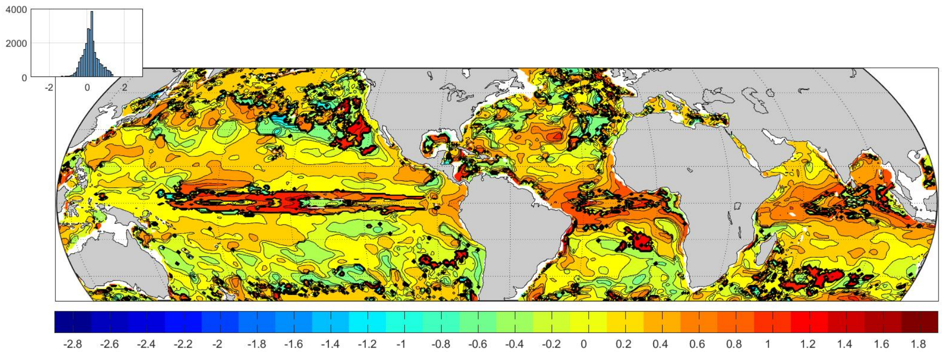

Fig. A2. $\log(P_a)$, years^2, from the fit of the exponential frequency term in the analytic spectrum. A low latitude and western dominance is the most conspicuous feature along with a high latitude intricacy. Fit is unstable in the equatorial Pacific and the contouring is incomplete there.

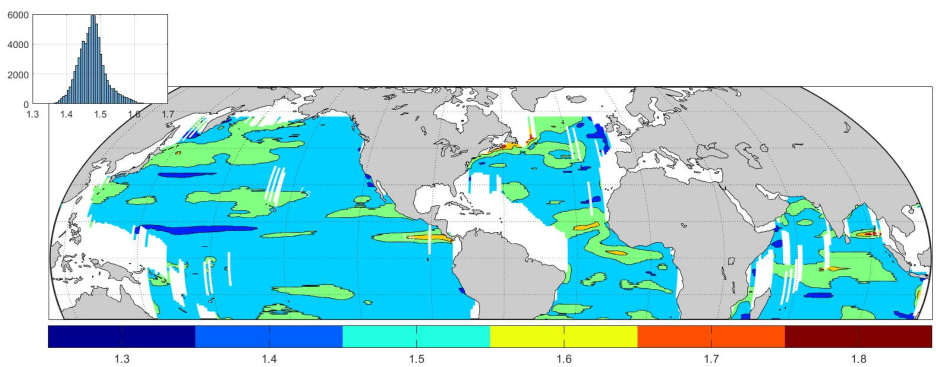

Fig. A3. Value α as the best fit in the meridional wavenumber spectrum, and dominated by a value near $\alpha = 3/2$.

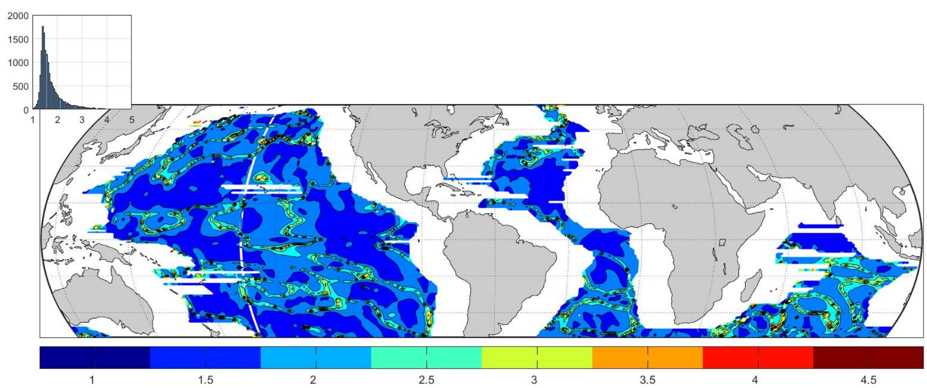

Fig. A4. Estimated value of α from the fit to the zonal wavenumber spectrum. These values are more nearly constant near the median of $\alpha = 1.6 \approx 3/2$.